



Structural, optical and vacancies investigations of Li-doped ZnO

Parasmani Rajput[✉] · Manvendra Kumar · Rucha S. Joshi · Prashant Singh · Mangla Nand · Rishabh Srivastava · Yash Patidar · Shiv Kumar · Archana Sagdeo · P. R. Sagdeo · Mukul Gupta · Fouran Singh · Saif A. Khan · P. Mondal · A. K. Srivastava · D. Bhattacharyya · S. N. Jha

Received: 24 February 2022 / Accepted: 13 July 2022 / Published online: 26 July 2022
© The Author(s), under exclusive licence to Springer Nature B.V. 2022

Abstract We have synthesised undoped and Li-doped ZnO by co-precipitation method and solid-state route resulting in ZnO ($Zn_{1-x}Li_xO$; $x=0, 0.03, 0.05, 0.08$) nanostructures (NSs) and bulk ZnO ($Zn_{1-x}Li_xO$; $x=0, 0.05, 0.1$), respectively. To examine the structural and optical properties, oxygen vacancies and local disorder, X-ray diffraction (XRD), scanning electron microscopy (SEM), transmission electron microscopy (TEM), diffuse reflectance spectroscopy (DRS), photoluminescence spectroscopy (PL), X-ray absorption fine structure

(XAFS) spectroscopy, X-ray photoelectron spectroscopy (XPS) and valence band spectra techniques were utilized. XRD confirms wurtzite structure for both undoped and Li-doped ZnO bulk and NSs samples. The undoped ZnO NSs show granular structures, while Li-doped ZnO NSs showed flake-like structures as elucidated by SEM. The flake dimension increases with increasing the Li content in the ZnO NSs, whereas the thickness of the flakes seems to be independent of the Li concentration. A reduction in particle size with Li doping was observed

P. Rajput (✉) · M. Nand · S. N. Jha
Beamline Development and Application Section, Bhabha Atomic Research Centre, Trombay, Mumbai 400085, India
e-mail: parasmanim80@gmail.com

P. Rajput · A. Sagdeo · A. K. Srivastava ·
D. Bhattacharyya · S. N. Jha
Homi Bhabha National Institute, Anushakti Nagar,
Mumbai 400094, India

M. Kumar (✉) · R. S. Joshi · R. Srivastava · Y. Patidar
Department of Physics, Institute of Science, Shri Vaishnav Vidyapeeth Vishwavidyalaya, Indore 453111, India
e-mail: kmanav@gmail.com

P. Singh
Department of Applied Sciences and Humanities, Institute of Engineering and Technology, Dr. Rammanohar, Lohia Avadh University, Ayodhya 224001, India

S. Kumar
Hiroshima Synchrotron Radiation Center, Hiroshima University, Hiroshima 739-0046, Japan

A. Sagdeo · P. Mondal · A. K. Srivastava
Synchrotrons Utilization Section, Raja Ramanna Centre for Advanced Technology, Indore 452013, India

P. R. Sagdeo
Material Research Laboratory (MRL), Department of Physics and MEMS, Indian Institute of Technology Indore, Simrol, Indore 452020, India

M. Gupta
UGC-DAE Consortium for Scientific Research, University Campus, Khandwa Road, Indore 452017, India

F. Singh · S. A. Khan
Inter University Accelerator Centre, Aruna Asaf Ali Marg, New Delhi 110067, India

D. Bhattacharyya
Atomic & Molecular Physics Division, Bhabha Atomic Research Center, Trombay, Mumbai 400085, India

from TEM for Li-doped ZnO NSs samples, which is consistent with the average crystallite size deduced from XRD. Bulk undoped ZnO shows nearly cuboid shape particles and the size of the particles increases with increasing Li content in ZnO. A blue shift in the optical band gap was obtained for Li-doped ZnO NSs, whereas a red shift is observed for Li-doped ZnO bulk. Band gap decreases with the incorporation of Li in ZnO bulk, while no further increase in band gap was observed for bulk ZnO after higher doping of Li. The oxygen vacancies in Li-doped ZnO bulk and NSs were observed by PL spectra, which were further corroborated by XAFS and oxygen vacancies are increased with an increase in the Li concentration in ZnO for both bulk as well as NSs samples. From the XPS study, it is confirmed that the oxygen vacancies for Li-doped ZnO NSs samples are increasing more as compared to Li-doped ZnO bulk samples. From DRS and valence band studies, it has been revealed that Li-doped bulk ZnO has band gap narrowing, whereas Li-doped ZnO NSs show band gap widening.

Keywords ZnO · Li doped · Luminescence · Band gap · Local structure · Vacancies, XAFS

Introduction

Zinc oxide (ZnO) has received excessive interest over the last two decades due to its unique and interesting chemical and physical properties. For example, it has large (60 meV) exciton binding energy, wide and direct band gap of 3.37 eV, high refractive index and piezoelectricity, etc. These characteristics make it one of the most important and essential multifunctional semiconductor materials for various applications such as solar cells, spintronic devices, transducers, gas sensors, photocatalysts and laser diodes, light emitting diodes (LED), etc. [1–4]. However, ZnO exhibits both n-type and p-type semiconductivity; therefore, it is an important material for high-quality optoelectronic devices. Due to zinc interstitials or oxygen vacancies native defects, ZnO naturally shows n-type conduction. However, getting p-type ZnO is rather tough because native defects result in self-compensation of acceptors [5, 6].

Various studies have been reported on the realisation of p-type conductivity in ZnO either by incorporation of group I elements on Zn-site or group V elements on oxygen-site [7, 8]. It has been observed that p-type ZnO can be achieved by Li doping [9, 10]. When Li gets absorbed on Zn-site, it acts as an acceptor but when it gets absorbed at the interstitial site (Li_i) then it acts as a donor [11]. However, Li^{1+} has a small ionic radius $\sim 0.60 \text{ \AA}$ as compared to Zn^{2+} ($\sim 0.74 \text{ \AA}$) because of which it can easily occupy different lattice positions. The p-type conductivity can be realized in ZnO by forming shallow acceptor states in substitutional zinc sites because of the incorporation of Li. Chawla et al. observed ferromagnetism in Li-doped ZnO nanorods with Curie temperature up to 554 K [12]. The antibacterial effect of ZnO nanowires can be considerably enhanced by Li doping [13]. Alexandrov et al. showed that the incorporation of Li, Ga and Mg in zinc oxide nanoparticles used as electron transport layer material for quantum dot light-emitting diodes led to a reasonable enhancement of the device properties [14]. By the first-principles method, it was reported that the Li doping in Zn improves photocatalytic properties [15]. Yadav et al. reported the removal of abiotic contaminants using Li-doped ZnO nanostructures [16]. From the various reports on Li-doped ZnO, it has been observed that structural, optical and electrical properties depend on preparation condition, particle size, formation of oxygen vacancies, etc. [17]. Lu et al. showed that the amount of Li doped into ZnO and the relative concentrations of Li substitutions and interstitials etc. play a crucial role in determining the conductivity of doped ZnO films [18]. On the other hand, diamagnetic behaviour was observed for un-doped ZnO, whereas room-temperature ferromagnetism can be induced after Li-doping in ZnO [19]. Li-doped ZnO showed significant improvement in photocatalytic activity [20] and luminescence properties [21]. Ariza et al. reported improved crystallinity up to some Li content with degradation in crystallinity due to further. They showed similar behaviour in the increase of the luminescent intensity in the visible range associated with the presence of defects [22]. Li doping not only can enhance/modify the properties of ZnO NSs but can also change the properties of ZnO thin films. Meziane et al. reported Li-doped and undoped ZnO thin films by the sol-gel method and optical results revealed an improvement of the total transmission when

increasing the Li amount [23]. Ultraviolet photo-response properties of Li-doped ZnO thin films prepared by the sol–gel spin-coating method have been reported by Lee et al. Where it is demonstrated that the Li doping in ZnO may lead to the development of sensors with the reduced rise and decay time and high sensitivity [24]. The defect present in the ZnO materials and the structure formed are mainly responsible for the alternation of the electrical and optical properties and are key parameters to optimize the performance of the device. Two kinds of emissions can be seen for the ZnO: ultraviolet near-band-edge emission and visible deep-level emission. The ultraviolet near-band-edge emission is observed at 380 nm and the visible deep-level emission can be observed in the range from 450 to 730 nm [25–27]. These emissions are related to the vacancies, interstitials, and anti-sites of Zn and O in ZnO. V_o , V_o^+ and V_o^{++} are responsible for the green emission and originated due to the transition from the conduction band to the deep levels of oxygen vacancies. On the other hand, the transitions from the conduction band to O_i levels result in orange emission and red emission due to the transition from zinc interstitial (Zn_i) to O_i . Different chemical routes were used for ZnO synthesis, such as the co-precipitation method, solution combustion, hydrothermal processes, the sol–gel method and the solid-state reaction process [17–21, 28–34]. We have used a solid-state synthesis route for undoped and Li-doped bulk ZnO and the co-precipitation method for the undoped and Li-doped ZnO NSs. Although co-precipitation is a time-consuming process, it offers a lot of advantages such as simple and rapid preparation, high yield, easy control of particle size and composition, control of overall homogeneity, high product purity and does not require high temperature and organic solvent. Several researchers have studied Mg, Ni, Fe and Mn-doped ZnO local structure using XAFS [35–38], but Li-doped ZnO local structure studies and its correlation with optical and vacancies are first time reported in this study.

In the present work, we have prepared Li-doped ZnO using two different methods and studied the influence of doping on its structural, surface, optical and vacancies studies using X-ray diffraction (XRD), diffuse reflectance spectroscopy (DRS), X-ray absorption fine structure spectroscopy (XAFS), scanning electron microscopy (SEM), transmission electron microscopy (TEM), photoluminescence spectroscopy

(PL), X-ray photoelectron spectroscopy (XPS) and valence band spectra techniques.

Experimental details

Synthesis of bulk ZnO

The Li-doped ZnO bulk ($Zn_{1-x}Li_xO$; $x=0, 0.05, 0.1$) were prepared by solid-state synthesis route, whereas Li-doped ZnO ($Zn_{1-x}Li_xO$; $x=0, 0.03, 0.05, 0.08$) NSs were prepared using co-precipitation method. For the synthesis of Li-doped ZnO bulk samples using the solid-state synthesis route, desired stoichiometry of Li=0, 0.05, 0.1, the appropriate proportion of high purity (>99.9% AR grade from Sigma-Aldrich) powder of ZnO and Li_2CO_3 properly mixed in liquid medium (propanol). After 3–4 h homogeneous mixing, the powder was calcined at 900 °C for 4 h.

Synthesis of ZnO NSs

The undoped and Li-doped ZnO NSs samples were synthesised using the co-precipitation method, where Zinc acetate dihydrate [$Zn(CH_3COO)_2 \cdot 2H_2O$], Lithium chloride (LiCl) and Potassium hydroxide (KOH) chemicals, from Merck India, have been used. All the chemicals were of AR grade and ready to use for the reaction without any preceding treatment. For the synthesis of the pure ZnO NSs sample, we have prepared two solutions simultaneously, named Solution A and Solution B. For Solution A, we have taken zinc acetate (2 mM ~0.4430 g) in methanol (100 mL) and then the mixture is kept on a hotplate magnetic stirrer for 2 h at room temperature to dissolve with continuous stirring. While for preparation of Solution B, 4 mM (0.2244 g) KOH was added in methanol (100 mL) with refluxing through a water condenser and a continuous stirring was performed for 2 h at 50 °C using another hotplate magnetic stirrer. Then, a mixed solution was prepared by mixing the solutions A and B and a constant stirring was maintained for 2 h. Refluxing through a water condenser was used at 50 °C to mix both the solutions. After 2 h of stirring, the solution was kept aside to reach room temperature and then aged overnight (~14 h). After centrifuging this solution, we washed the centrifuged materials with absolute ethanol and water several times to eliminate contaminations. White powders of ZnO were

obtained after 24 h keeping the materials in a vacuum oven at 50 °C.

For the preparation of Li-doped ZnO NSs, the equivalent weight of Li for doping percentage was dissolved in 15 mL of methanol with continuous stirring at room temperature and then mixed with the 85 mL of Zinc acetate solution with an appropriate mole of Zn to Li. Now, freshly prepared KOH solution was added to this solution and all the other procedures were the same as described for the synthesis of undoped ZnO NSs. For example, zinc acetate dihydrate (0.4297 g), lithium chloride (0.0026 g) and KOH (0.2244 g) were used for the synthesis of 3% Li-doped ZnO.

Characterizations

Structure analysis of all the powder samples was performed by XRD technique using laboratory X-ray source, on Bruker D8 Advance diffractometer having Cu target and LYNXEYE detector. DRS measurements were carried out using Carry-60 UV-VIZ-NIR spectrophotometer to get information about the optical band gap of all the samples in the wavelength range of 190 nm to 800 nm. Zn K-edge measurements were done in transmission mode at scanning extended X-ray absorption fine structure (EXAFS) beamline (BL-9) and O K-edge were done in total electron yield mode at soft X-ray absorption spectroscopy beamline (BL-1) at Indus-2. The XAFS spectrum for Zn-foil (as reference) was also recorded in the same setup for energy calibration. The analysis of the XAFS data was carried out using the FEFF 6.0 code [39] with the help of ATHENA software [40, 41]. ARTEMIS software was used to generate the theoretical XAFS spectra from an expected crystallographic structure [40, 41]. The best fit of XAFS data was obtained to minimize R_{factor} in the fitting procedure [42].

MIRA II LMH from TESCAN field emission scanning electron microscope (FE-SEM) was used to investigate the surface morphology. The energy of electrons was kept at 25 keV and images were captured using the secondary electron detector. To get a TEM image, we used a Philips CM200 system. The powder sample was dispersed in a deionized (DI) water medium by ultrasonication. These dispersed particles were lifted on copper TEM grids for the characterization.

For the PL measurements, a 100 mW power-operated HeCd laser (KIMMON, Japan) was used and spectra were recorded by an Ocean Optics (HR4000) spectrometer at room temperature under 325 nm excitation wavelength.

The valence band (VB) spectra were recorded at angle-resolved photoelectron spectroscopy (ARPES) beamline, BL-3, of Indus-1 using a synchrotron radiation source with 60 eV photon energy, whereas O 1s core-level spectra were recorded using Al K α X-ray source. All the spectra were recorded in step size of 0.05 eV and with a pass energy of 30 eV. A SPECS Phoibos 150 HV hemispherical electron analyzer was used for VB measurements. It is mounted on the UHV chamber (base pressure $\sim 5 \times 10^{-9}$ mbar) in the horizontal direction, at 45° from the incoming X-ray beam. All the XPS spectra were calibrated to the binding energy of C 1s (284.6 eV) core level as reference. The doping percentage of Li in ZnO was confirmed using XPS measurements and found to be the same as expected.

Results and discussion

X-ray diffraction

XRD patterns of undoped and Li-doped ZnO bulk and NSs are presented in Figs. 1 and 2, respectively. The diffraction peaks appearing at angles (2 θ) of 31.8°, 34.5°, 36.3°, 47.6°, 56.7°, 62.9°, 66.5°, 68.1°, 72.6° and 77.1° corresponding to the reflection from the (1 0 0), (0 0 2), (1 0 1), (1 0 2), (1 1 0), (1 0 3), (2 0 0), (1 1 2), (2 0 1), (0 0 4) and (2 0 2) planes, respectively, are the crystal planes of the hexagonal wurtzite ZnO structure (JCPDS 36–1451, 89–7102). The Rietveld refinement of $\text{Zn}_{1-x}\text{Li}_x\text{O}$ ($x=0, 0.03, 0.05, 0.08$) NSs are also performed as shown in Fig. 1a–d. XRD patterns confirmed that with Li doping the structure remains in the wurtzite structure with preferred orientation along (101) and no trace of any impurity peak is observed. The lattice parameters obtained from XRD fitting are $a=b=3.249$ Å and $c=5.203$ Å for Li-doped ZnO NSs and $a=b=3.252$ Å and $c=5.209$ Å for Li-doped ZnO bulk, respectively. It has been observed that XRD peaks get broadened with increasing Li concentration in NSs. The crystal size of all the samples was calculated by Scherrer's formula using (101) plane diffraction peak. For the

increasing Li concentrations from 0 to 0.03, 0.05 and 0.08 in NSs, the crystal size decreased from 10.8 to 8.79, 8.82 and 7.66 nm, respectively. The bulk ZnO undoped sample has a crystal size of ~104.7 nm as calculated from Scherrer's equation. After doping, the crystal size has been increased to 168.5 nm for 0.03 Li doping, followed by a reduction in the crystal size with further Li incorporation in ZnO bulk. The crystal sizes are 159.7, 145.7 and 114.3 nm for 0.05, 0.08 and 0.1 Li concentration in ZnO bulk. We have also calculated the strain in ZnO NSs using Williamson-Hall (WH) plot as shown in Fig. 3. The strain has been found to increase after Li doping. The results are given in Table 1. The reduction of crystal size with Li doping in NSs and bulk is induced by the smaller ionic radius (0.68 Å) of Li⁺ as compared to ionic radii of Zn²⁺ ions (0.74 Å) [43]. Thus, the incorporation of Li atoms in the interstitial site progressively reduces the concentration of Zn in the system. Hence, Li atoms are segregated at the grain boundaries resulting in a reduction in the crystallite size. The Fujihara et al. has also reported similar results [44].

Scanning electron microscopy and transmission electron microscopy

The surface morphology of ZnO NSs and bulk were investigated by SEM as shown in Figs. 4 and 5 at different magnifications, respectively. The SEM results

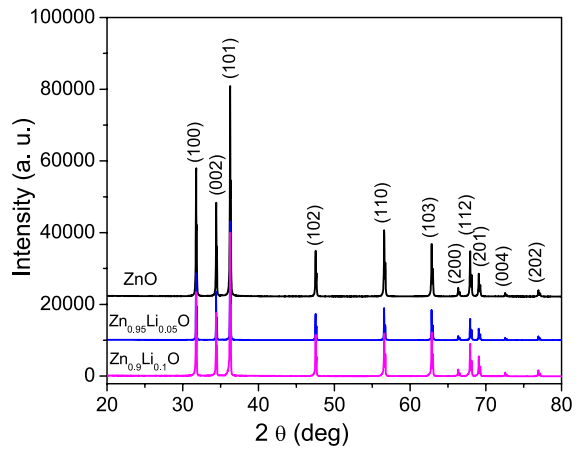
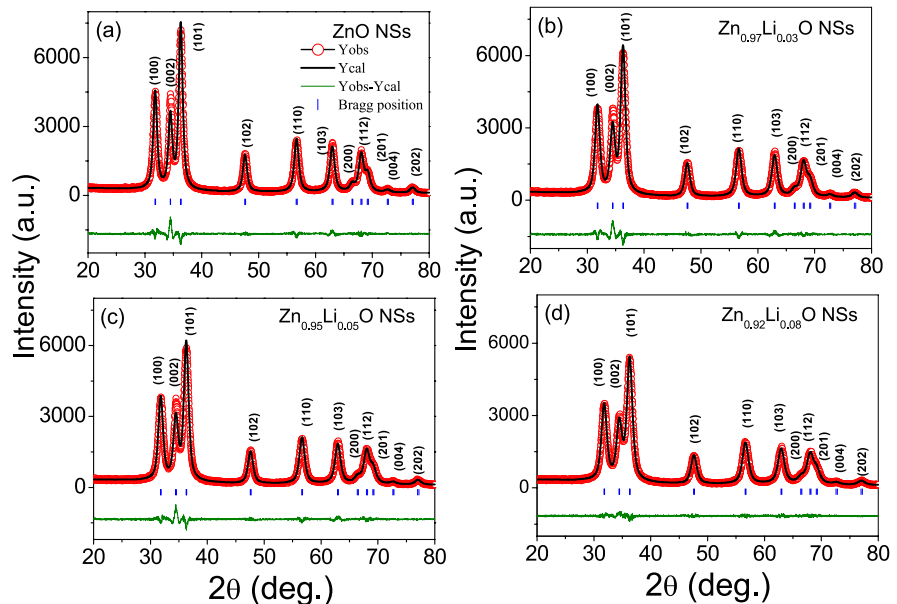


Fig. 2 X-ray diffraction pattern of Zn_{1-x}Li_xO (x=0, 0.05, 0.1) bulk. The patterns are shifted in y-scale for the sake of clarity

confirm that undoped ZnO NSs have granular structures with ~20 nm diameter, whereas after Li doping in ZnO, flake like nanostructures are observed. The observed flake like nanostructures are uniform in size and homogeneously distributed. The dimensions of the flake like nanostructures are in the range of 250–730 nm, 270–1170 nm and 380–990 nm having a thickness in the range of ~15–40 nm for ZnO NSs doped with 0.03, 0.05, 0.08 Li content, respectively. The flake thickness in Li-doped ZnO NSs samples appears to be independent of the Li doping

Fig. 1 a–d Rietveld refined X-ray diffraction pattern of Zn_{1-x}Li_xO (x=0, 0.03, 0.05, 0.08) NSs



percentage. Bulk undoped ZnO shows nearly cuboid shape particles with dimensions in the range of 100–750 nm and Li-doped ZnO bulk samples show nearly spherical particles with dimensions in the range of 16–22 μm . To obtain more details about the structures of NSs samples, TEM measurements were performed and the results are shown in the left panel of Fig. 6. The selected area electron diffraction (SAED) patterns are shown in the right panel of Fig. 6 indicating the wurtzite structure of prepared ZnO which is consistent with XRD results. The particle size distribution, deduced from TEM images by taking approximately 100 particles from each image, is shown in Fig. 7. One can observe a better size distribution with an increase in the Li doping percentage as depicted from the distribution profile. The average

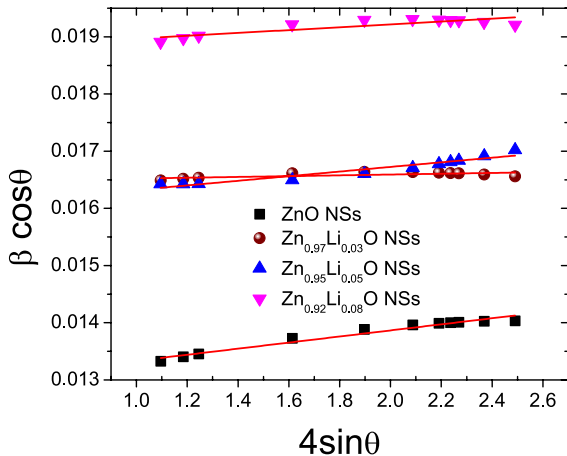
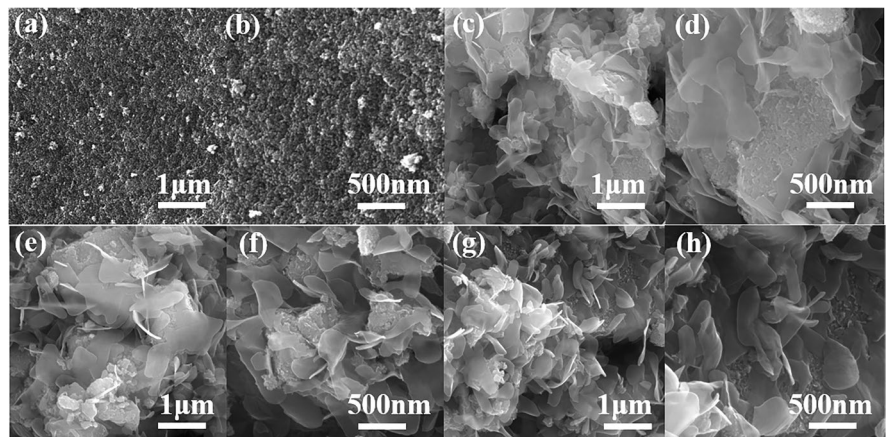


Fig. 3 Williamson-Hall plot corresponding to $\text{Zn}_{1-x}\text{Li}_x\text{O}$ ($x=0, 0.03, 0.05, 0.08$) NSs

Fig. 4 FE-SEM micrographs of **a, b** ZnO NSs, **c, d** $\text{Zn}_{0.97}\text{Li}_{0.03}\text{O}$ NSs, **e, f** $\text{Zn}_{0.95}\text{Li}_{0.05}\text{O}$ NSs and **g, h** $\text{Zn}_{0.92}\text{Li}_{0.08}\text{O}$ NSs samples

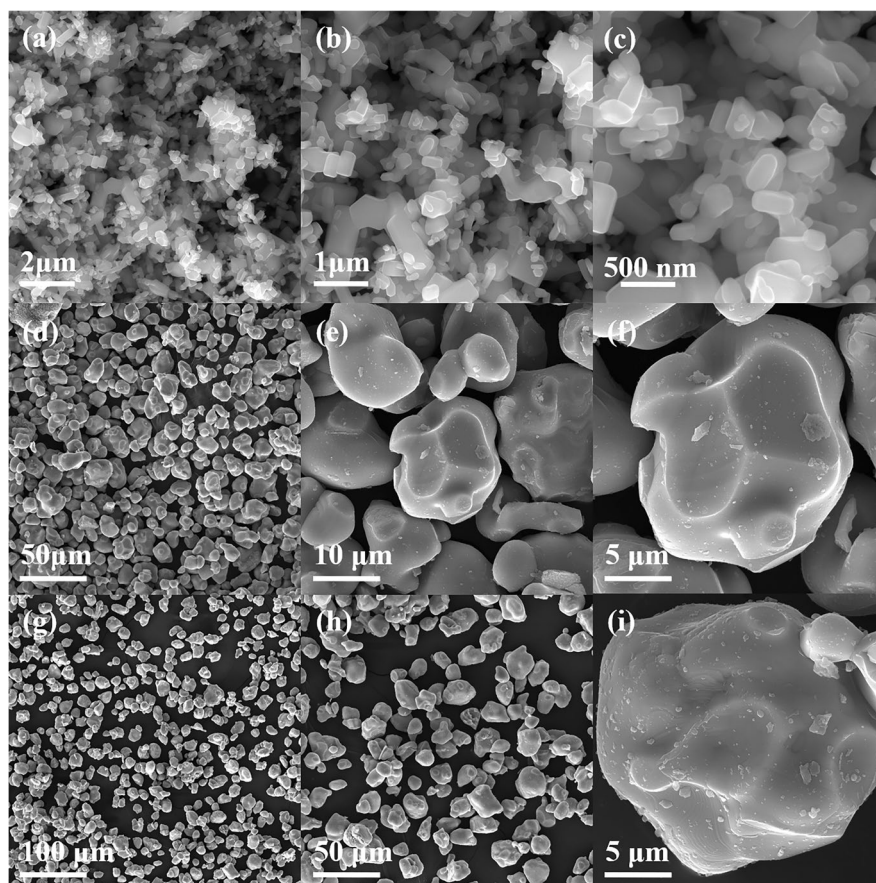


particle size was calculated by Gaussian fit of the distribution profile and a decrease in nanoparticle size was obtained for $\text{Zn}_{0.97}\text{Li}_{0.03}\text{O}$ and $\text{Zn}_{0.92}\text{Li}_{0.08}\text{O}$ NSs samples. The deduced average particle sizes are 13.6, 8.2 and 7.7 nm for undoped and 0.05% and 0.08% Li-doped ZnO NSs, respectively. One can also see the better size distribution with a higher percentage of Li incorporation in ZnO NSs. The average crystal sizes calculated from Scherrer's equation and Williamson-Hall plot perfectly match the size deduced from TEM analysis as shown in Table 1.

Diffuse reflectance spectroscopy

The band gap in undoped, Li-doped ZnO bulk and NSs was calculated from DRS spectra using the Kubelka-Munk plot [45]. Figure 8 shows a plot between $[F(R_\infty) \times hv]^2$ and hv for $\text{Zn}_{1-x}\text{Li}_x\text{O}$ bulk and NSs samples. The E_g values were obtained by extrapolating the linear fit of $[F(R_\infty) \times hv]^2$ curves as a function of hv to intercept value on the energy axis as shown by the arrow line in Fig. 8. The obtained E_g values are 3.24, 3.16, 3.16 eV corresponding to the ZnO bulk, $\text{Zn}_{0.95}\text{Li}_{0.05}\text{O}$ bulk, $\text{Zn}_{0.9}\text{Li}_{0.1}\text{O}$ bulk and 3.27, 3.3, 3.3, 3.33 eV corresponding to the undoped ZnO, $\text{Zn}_{0.97}\text{Li}_{0.03}\text{O}$, $\text{Zn}_{0.95}\text{Li}_{0.05}\text{O}$ o and $\text{Zn}_{0.92}\text{Li}_{0.08}\text{O}$ NSs, respectively. For Li-doped NSs, it has been observed that the band gap increases as Li concentration increases. This widening (blueshift) of the optical band gap is mainly attributed to the Burstein-Moss effect (B-M) [46]. As the Li doping increases in NSs, there is an increase in the charge carrier concentration and the Fermi level merges into the

Fig. 5 FE-SEM micrographs of **a, b, c** ZnO bulk, **d, e, f** $\text{Zn}_{0.95}\text{Li}_{0.05}\text{O}$ bulk and **g, h, i** $\text{Zn}_{0.9}\text{Li}_{0.1}\text{O}$ bulk samples



conduction band. On the other hand, Li-doped bulk samples show band gap narrowing (red shift). This reduction of band gap for bulk ZnO is due to the combined effect of the conduction-band renormalization [47] and the B-M effect [46]. There is another possible reason for the red shift in band gap for bulk samples which may be due to the oxygen vacancies and defects in the host lattice [48]. The band gap widening and narrowing with the same element doping can be understood in terms of the size of crystallites and the shape of the particles. A similar result of size- and shape-dependent band gap has also been reported by N. Kamarulzaman et al. [49]. These results are further supported by valence band studies.

X-ray absorption near edge structure and X-ray absorption fine structure

Figure 9a, b shows normalized Zn K-edge spectra of $\text{Zn}_{1-x}\text{Li}_x\text{O}$ ($x=0, 0.05, 0.1$) bulk and $\text{Zn}_{1-x}\text{Li}_x\text{O}$

($x=0, 0.05, 0.08$) NSs samples. The Zn K-edge XANES spectra confirm that Zn is in 2+ oxidation state in all the samples. With Li-doped ZnO bulk as well as NSs samples, there is no change in oxidation state which confirms that Li ions occupy the Zn ions sites in the wurtzite structure and no impurity phase appears. Interestingly, it has been observed that there is a reduction of a white line intensity with Li-doped ZnO bulk as well as NSs. This reduction of white line mainly arises due to the variation of charge transfer upon Li doping. A similar reduction of a white line on Ni doping in ZnO was also observed by Rana et al. [36]. The O K-edge XANES spectra of $\text{Zn}_{1-x}\text{Li}_x\text{O}$ ($x=0, 0.05, 0.1$) bulk and $\text{Zn}_{1-x}\text{Li}_x\text{O}$ ($x=0, 0.05, 0.08$) NSs samples are shown in Fig. 10a, b. O K-edge mainly probes unoccupied states in the conduction band by the transitions of O 1s electron into O 2p states which are hybridized with neighbouring metals. The features A, B and C are mainly due to transitions into O 2p states hybridized with Zn

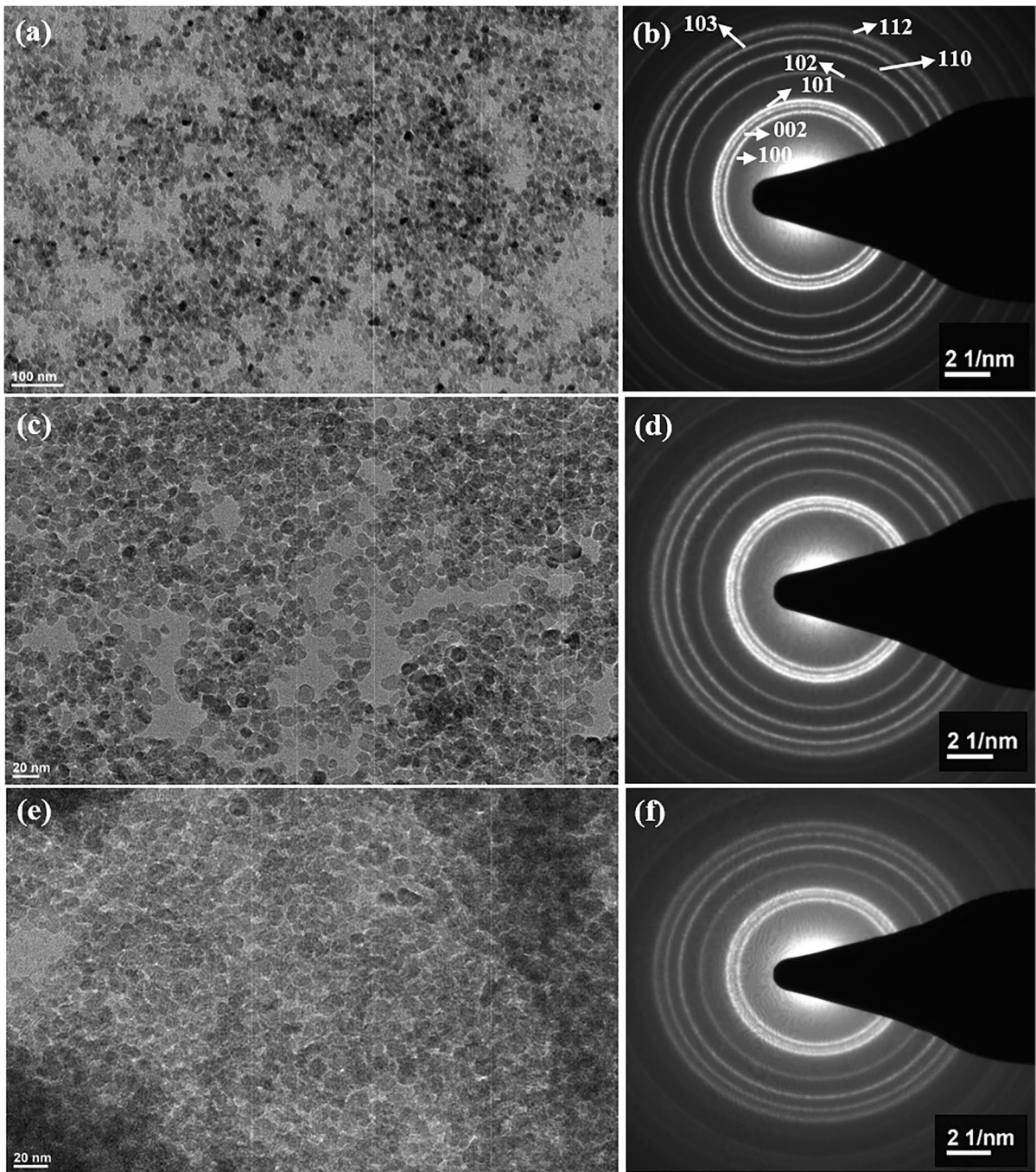


Fig. 6 TEM images of **a** ZnO NSs, **c** $\text{Zn}_{0.95}\text{Li}_{0.05}\text{O}$ NSs and **e** $\text{Zn}_{0.92}\text{Li}_{0.08}\text{O}$ NSs samples. **b**, **d**, **f** are the SAED patterns, respectively

4 *s* states [50]. Features D and E are due to O 2*p* states hybridized with Zn 4*p* states, whereas feature F is due to O 2*p*-Zn 4*d* hybridized states [50]. As shown in Figure 10a, b, O K-edge spectra shows

all (A–F) features for $\text{Zn}_{1-x}\text{Li}_x\text{O}$ ($x=0, 0.05, 0.1$) bulk and $\text{Zn}_{1-x}\text{Li}_x\text{O}$ ($x=0, 0.05, 0.08$) NSs samples. Interestingly, feature A corresponding to pre-edge shows significant enhancement in intensity in

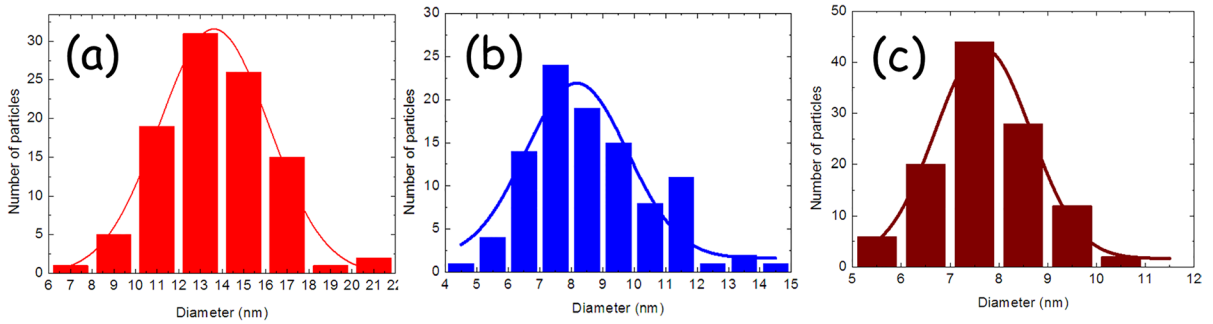
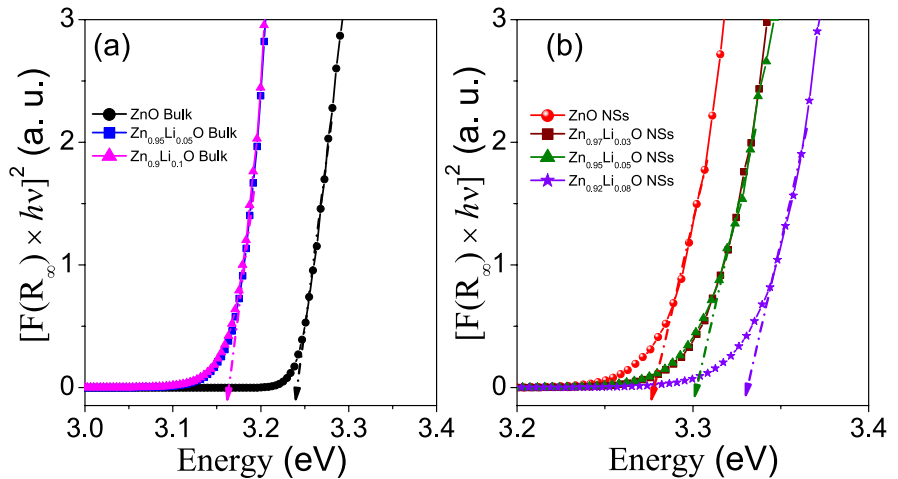


Fig. 7 The particle size distribution deduced from TEM images for Li doping percentages **a** 0, **b** 0.05 and **c** 0.08% NSs

Table 1 Crystal size and strain calculated by Scherrer’s equation, TEM analysis and Williamson-Hall plot for Li-doped NSs and Bulk ZnO

Li concentration	Crystal Size (nm): ZnO bulk	Crystal size (nm) and strain: ZnO NSs			Particle size (nm): ZnO NSs TEM
		Scherrer’s equation	Scherrer’s equation	Williamson-Hall Plot	
0	104.7	10.88	10.8	5.32339E-4	13.6
0.03	168.5	8.79	8.4	4.73878E-5	–
0.05	159.7	8.82	8.7	7.06427E-5	8.2
0.08	145.7	7.66	7.4	9.24346E-5	7.7
0.1	114.3	–	–	–	–

Fig. 8 The Kubelka–Munk plot as a function of energy for **a** $Zn_{1-x}Li_xO$ ($x=0, 0.05, 0.1$) bulk and **b** $Zn_{1-x}Li_xO$ ($x=0, 0.03, 0.05, 0.08$) NSs. The band gap values have been determined using slope of straight line



Li-doped ZnO NSs compare to Li-doped ZnO bulk. This reveals that there is an increase in the unoccupied density of states corresponding to O 2p-Zn4s hybridization states in Li-doped ZnO NSs [51]. The variation in unoccupied density of states may be

due to variation in oxygen vacancies for Li-doped ZnO NSs and Li-doped ZnO bulk. As we know that O K-edge is sensitive to surface information only, therefore, more investigations are needed to know oxygen vacancies behaviour in all the Li-doped

ZnO samples. However, Zn K-edge XAFS analysis was performed to know local vacancies corresponding to Zn–O and Zn–Zn atoms.

Figure 11a, b shows the best fit of magnitude and real component of the Fourier transform of Zn XAFS functions for $Zn_{1-x}Li_xO$ ($x=0, 0.05, 0.1$) bulk and $Zn_{1-x}Li_xO$ ($x=0, 0.05, 0.08$) NSs. The k -range of $2.5\text{--}9 \text{ \AA}^{-1}$ was used for Fourier transform, whereas the phase un-corrected R -space range of $1\text{--}3.21 \text{ \AA}$ was used for fitting. For Zn K-edge XAFS fitting, the structure is assumed as pure ZnO wurtzite, where Zn is co-ordinated with four O atoms (Zn–O) at 1.98 \AA distance in the first shell and second next near-neighbour Zn is bounded by 12 Zn atoms (Zn–Zn) at 3.21 \AA distance. The local structural parameters, i.e. coordination numbers, bond distances and Debye–Waller (DW) factor, as determined by these fittings are listed in Table 2. From the fitting of Zn K-edge XAFS, there is not much significant change

in Zn–O and Zn–Zn bond distance of undoped ZnO bulk and NSs. It has been observed from Zn K-edge XAFS analysis that Zn–O and Zn–Zn bond distance and disorder increase in $Zn_{0.95}Li_{0.05}O$ bulk and $Zn_{0.9}Li_{0.1}O$ bulk as compared to undoped ZnO bulk. For the Li-doped NSs, the Zn K-edge fitting confirms the reduction of coordination number and increase in Zn–O and Zn–Zn bond distances and disorder. It has been noticed from XAFS fitting that the bond distance of Zn–O and Zn–Zn of ZnO NSs are the same as ZnO Bulk. After doping Li in ZnO NSs and ZnO bulk, Zn–O and Zn–Zn bond distances are increased. The increase in bond distance with Li doping is due to the ionic radius of Li^+ (0.68 \AA) being less than Zn^{2+} (0.74 \AA) [43]. It has been observed that Zn–O and Zn–Zn coordination number for ZnO NSs has been reduced as compared to ZnO bulk, since a large number of atoms are occupied on the surface in form of NSs which is known as the

Fig. 9 Normalized Zn K-edge spectra of **a** ZnO bulk, $Zn_{0.95}Li_{0.05}O$ bulk and $Zn_{0.9}Li_{0.1}O$ bulk. **b** ZnO NSs, $Zn_{0.95}Li_{0.05}O$ NSs and $Zn_{0.92}Li_{0.08}O$ NSs samples

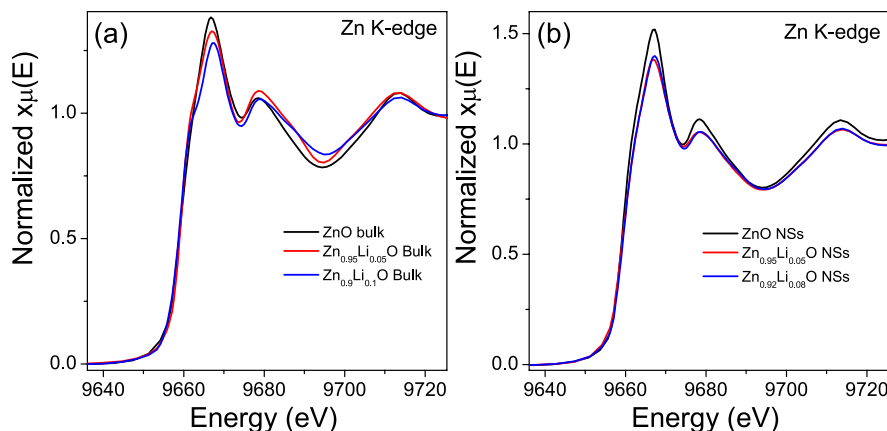
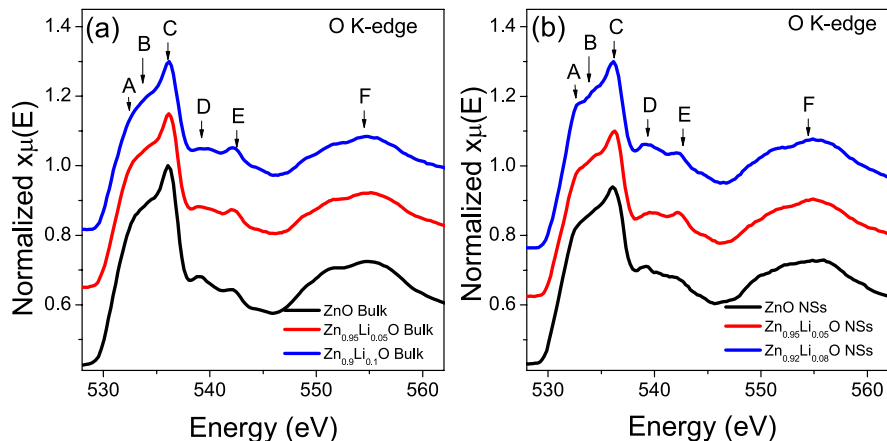


Fig. 10 O K-edge spectra of **a** ZnO bulk, $Zn_{0.95}Li_{0.05}O$ bulk and $Zn_{0.9}Li_{0.1}O$ bulk. **b** ZnO NSs, $Zn_{0.95}Li_{0.05}O$ NSs and $Zn_{0.92}Li_{0.08}O$ NSs samples. The data has been shifted vertically for sake of clarity



nano-size effect [52]. The decreased coordination number of Zn–O and Zn–Zn neighbouring atoms in Li-doped NSs indicates the presence of large oxygen vacancies. A similar decrease in coordination numbers with doping has also been observed by various workers [37, 38]. The increased oxygen vacancies with doping are observed due to a lower ionic radius; therefore, oxygen vacancies are formed at the host site, i.e. in the neighbourhood of Zn.

Photoluminescence spectroscopy

The PL spectra of the undoped ZnO (bulk and NSs), Li-doped bulk and NSs samples recorded at

the excitation wavelength of 325 nm are shown in Fig. 12. The emission spectrum of pure ZnO consists of two major peaks marked as A and B at ~388 nm (UV) and ~585 nm (green), respectively [53–57]. It is well known that the peak at ~388 nm corresponds to the band edge emission of ZnO, which originates due to the radiative recombination of the free exciton–exciton collision process in the ZnO. The band edge emission peak is absent for all the Li-doped ZnO Bulk samples. The disappearance of band edge emission in Li-doped ZnO bulk samples can be attributed either to the exciton pairs recombination at the non-radiative centres or to the increase in the density of defect. A close exploration of the band

Fig. 11 **a** Magnitude and **b** real component of the Fourier transform of XAFS functions ($k^2\chi(k)$) for $Zn_{1-x}Li_xO$ ($x=0, 0.05, 0.1$) bulk and $Zn_{1-x}Li_xO$ ($x=0, 0.05, 0.08$) NSs. Dotted lines represent the experimental data whereas the solid lines represent the best fit

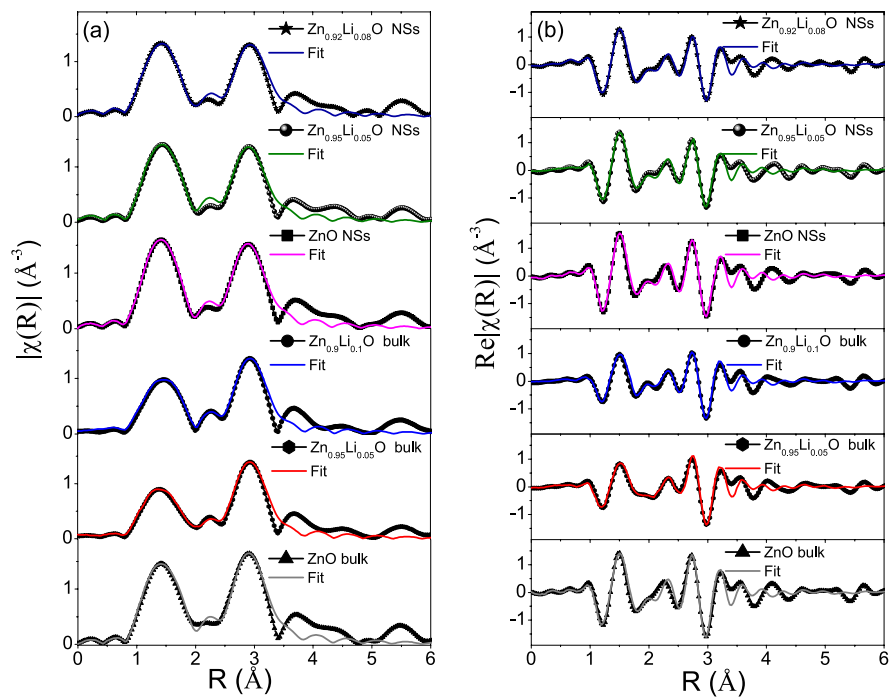
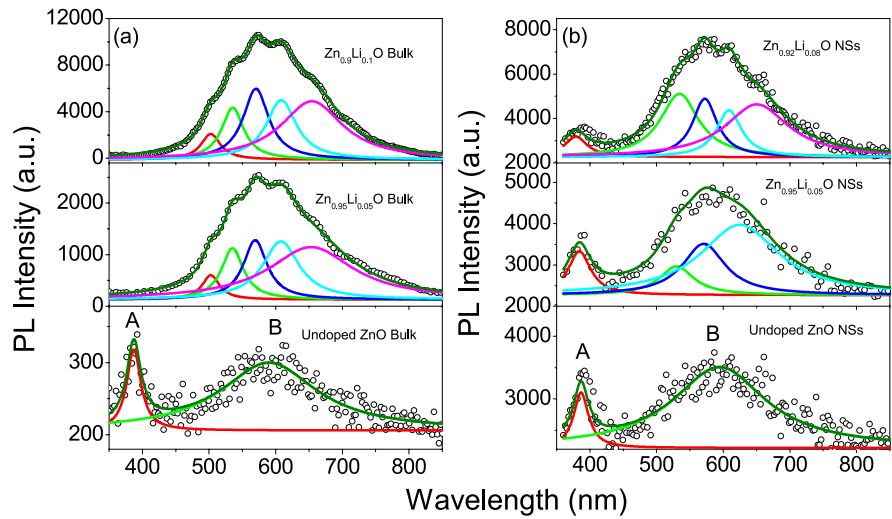


Table 2 Structural parameters obtained by fitting the experimental XAFS signals measured at the Zn K-edge. The CN is the coordination numbers, whereas R is the average inter-

atomic distance and σ^2 the EXAFS Debye–Waller factor. The numbers in parentheses indicate the uncertainty in the last digit

Sample	CN_{Zn-O}	$R_{Zn-O}(\text{Å})$	$\sigma^2_{Zn-O}(\text{Å}^2)$	CN_{Zn-Zn}	$R_{Zn-Zn}(\text{Å})$	$\sigma^2_{Zn-Zn}(\text{Å}^2)$
ZnO Bulk	4	1.919(3)	0.0084(3)	12	3.240(3)	0.0095(4)
$Zn_{0.95}Li_{0.05}O$ Bulk	4	1.924(3)	0.0163(4)	12	3.258(4)	0.0112(5)
$Zn_{0.9}Li_{0.1}O$ Bulk	4	1.944(4)	0.0157(5)	12	3.252(4)	0.0117(5)
ZnO NSs	3.6 (2)	1.916(3)	0.0052(3)	11.2(3)	3.238(3)	0.0095(4)
$Zn_{0.95}Li_{0.05}O$ NSs	3.3(3)	1.923(3)	0.0059(4)	10.4(3)	3.241(3)	0.0101(4)
$Zn_{0.92}Li_{0.08}O$ NSs	3.2(3)	1.929(3)	0.0061(3)	10.3(3)	3.261(4)	0.0102(4)

Fig. 12 Photoluminescence spectra of **a** ZnO bulk, $\text{Zn}_{0.95}\text{Li}_{0.05}\text{O}$ bulk and $\text{Zn}_{0.9}\text{Li}_{0.1}\text{O}$ bulk samples and **b** ZnO NSs, $\text{Zn}_{0.95}\text{Li}_{0.05}\text{O}$ NSs and $\text{Zn}_{0.92}\text{Li}_{0.08}\text{O}$ NSs samples. The black dots show experimental data, green lines Gaussian fitting and red line sum of all fitted peaks



edge emission band in NSs samples suggests a blue shift in the band position, which shifted from 387.5 to 380.8 nm when Li doping was changed from 0 to 0.08%. The band position of 0.05% Li doped ZnO is at 385.5 nm. Also, the intensity of band edge emission was found to increase with the concentration of Li and can be related to the decrease in the size of the particles. The broad band B is comprised of several different bands having a central peak position at ~ 572 nm, which is also slightly blue-shifted as compared to the pure ZnO sample. This visible band is composed of multiple electronic transitions which is originated due to the overlapped emission of green, yellow, orange and red emissions.

The broad visible band present the PL spectra of all the doped sample that can be de-convoluted into five peaks, labelled as 1, 2, 3, 4 and 5, using Lorentzian function in Origin, corresponding to neutral oxygen vacancies (V_{O}), single charge oxygen vacancies (V_{O}^+), double charge oxygen vacancies (V_{O}^{++}) and oxygen interstitials (O_i). V_{O} (536 nm), V_{O}^+ (572 nm) and V_{O}^{++} (612 nm) are responsible for the green emission and originated due to the transition from the conduction band to the deep levels of oxygen vacancies. On the other hand, the transitions from the conduction band to O_i levels result in orange emission (670–720 nm) and red emission (720–780 nm) is obtained due to the transition from zinc interstitial (Zn_i) to O_i . [27].

Figure 13 shows variation in the integrated areal PL intensity with Li concentration for the bulk and NSs samples. The PL intensity for $\text{Zn}_{0.95}\text{Li}_{0.05}\text{O}$ bulk is ~ 32 times higher as compared to pure ZnO

bulk and that is ~ 128 times higher for $\text{Zn}_{0.9}\text{Li}_{0.1}\text{O}$ bulk, whereas $\text{Zn}_{0.92}\text{Li}_{0.08}\text{O}$ NSs is ~ 12 times higher as compared to ZnO NSs. From the PL analysis, it has been observed that ZnO NSs samples have a greater number of oxygen vacancies as compared to ZnO bulk.

X-ray photoelectron spectroscopy and valence band spectra

Figure 14a, b shows the XPS O 1s core level spectra of ZnO bulk, $\text{Zn}_{0.9}\text{Li}_{0.1}\text{O}$ bulk, ZnO NSs

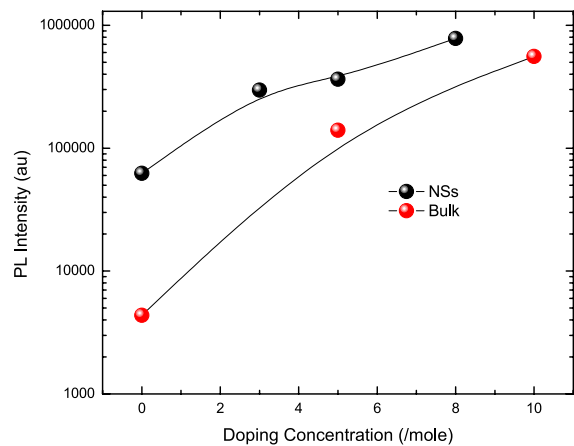
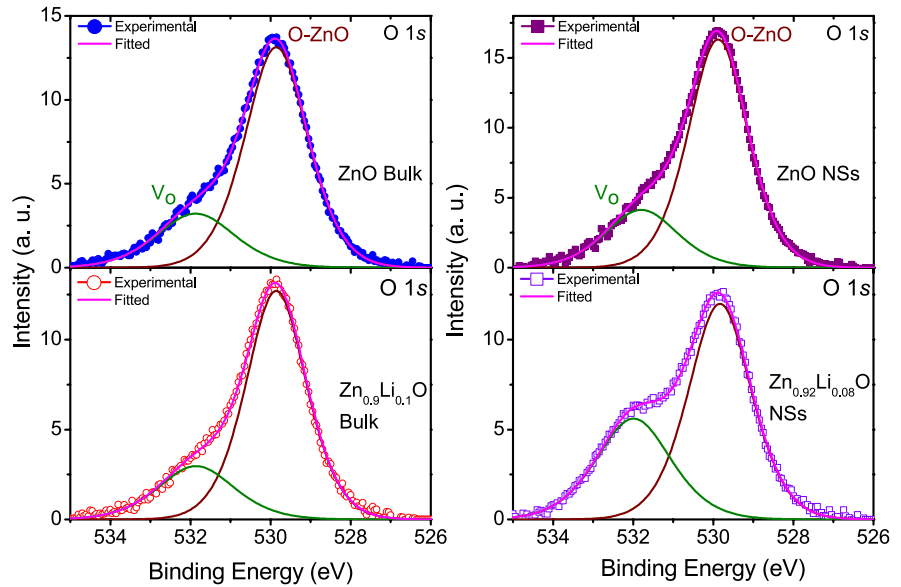


Fig. 13 PL intensity with Li concentration for the bulk and NSs samples

Fig. 14 O 1 s core level spectra of **a** ZnO bulk and Zn_{0.9}Li_{0.1}O bulk. **b** ZnO NSs and Zn_{0.92}Li_{0.08}O NSs samples

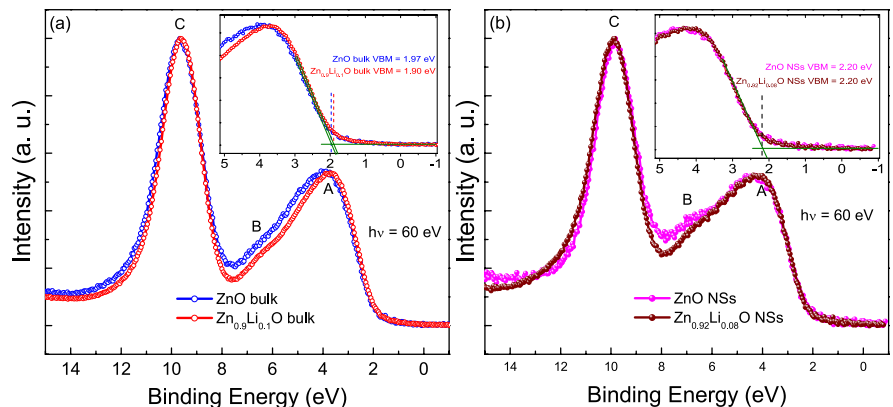


and Zn_{0.92}Li_{0.08}O NSs samples. The O 1 s spectrum shows an asymmetric shape and the presence of two peaks. From the fitting of O 1 s core level spectrum of ZnO, the peak position appears at 531.87 ± 0.05 eV and 529.86 ± 0.05 eV. The first peak of O 1 s is mainly associated with the O-ZnO bond and the second peak intensity is due to oxygen vacancies (V_o) in ZnO [58]. It has been observed that there is a drastic change in the intensity of oxygen vacancy peak corresponding to Li-doped NSs samples compare to Li-doped bulk samples. This confirms that there is a large increase in oxygen vacancies in Li-doped NSs samples as compared to Li-doped bulk samples.

The valence band spectra of ZnO bulk, Zn_{0.9}Li_{0.1}O bulk, ZnO NSs and Zn_{0.92}Li_{0.08}O NSs

samples were measured using 60 eV photon energy, as shown in Fig. 15a, b. The valence band spectra consist of three main features A, B and C. Peak A is the valence peak, B due to the hybridization of O 2p with Zn 4 s and Zn 4p states and C is mainly due to the Zn 3d states [59]. There is no binding energy shift that has been observed corresponding to feature B & C for all the samples. Interestingly, there is change in peak B intensity after Li doping in bulk as well as NSs attributed to the modification in the hybridization of energy levels in the presence of Li doping [60]. The valence band maximum (VBM) was determined using the linear extrapolation of the valence band edge and found to be 1.97 ± 0.05 eV for ZnO bulk, 1.90 ± 0.05 eV for Zn_{0.9}Li_{0.1}O bulk, 2.20 ± 0.05 eV for ZnO NSs and Zn_{0.92}Li_{0.08}O NSs,

Fig. 15 Valence band spectra of **a** ZnO bulk and Zn_{0.9}Li_{0.1}O bulk. **b** ZnO NSs and Zn_{0.92}Li_{0.08}O NSs samples. The inset represents enlarged view of valence band edge with VBM values



respectively. After Li doping $\text{Zn}_{0.9}\text{Li}_{0.1}\text{O}$ bulk, it has been found that there is a valence band shift towards the lower binding energy with respect to pure ZnO. Similarly, undoped and Li-doped $\text{Zn}_{0.92}\text{Li}_{0.1}\text{O}$ NSs show valence band shift towards the higher binding energy with respect to pure ZnO. It is also observed that there is a shift in peak position and width of Zn $3d$ after Li doping in ZnO which resembles the band narrowing and widening. The shift in Zn $3d$ peak depends on the electronic state of Li^+ and Zn^{2+} ions in Li-doped ZnO system, where Li and Zn are in +1 and +2 stable states, respectively. In the presence of Li^+ ions in the ZnO lattice, the shift of valence band spectra depends on how addition energy levels near and above are hybridized with the valence band. The VBM shift towards lower binding energy suggests that the valence band shifts towards the conduction band, whereas the VBM shift on higher binding energy confirms a large downward shift of the valence band. The upward shift of the valence band is due to the formation of additional fully occupied impurity bands above the valence band, ascribed as band gap narrowing [49] and accounting for a decrease in the band gap in $\text{Zn}_{0.9}\text{Li}_{0.1}\text{O}$ bulk. The downward shift of the valence band is mainly because the Fermi level (E_F) lies in the conduction band, ascribed as band gap widening and consequently band gap increases in undoped ZnO NSs and $\text{Zn}_{0.92}\text{Li}_{0.1}\text{O}$ NSs.

From the present study, we have found that the average particle size decreases with doping percentage as confirmed by XRD and TEM in ZnO NSs increasing the band gap which is opposite to the trend of band gap for bulk ZnO. From XAFS, we found that the disorder is more in bulk samples with respect to NSs samples. Photoluminescence studies indicate higher oxygen vacancies in NSs samples, which is also evident from the XPS investigations. On the other hand, the valence band results are consistent with band gap finding in both sets of samples.

Conclusion

Li-doped ZnO, ($\text{Zn}_{1-x}\text{Li}_x\text{O}$; $x=0, 0.05, 0.1$) bulk and ($\text{Zn}_{1-x}\text{Li}_x\text{O}$; $x=0, 0.03, 0.05, 0.08$) NSs have been prepared. XRD measurement revealed wurtzite structure for both types of samples. A blue

shift has been observed in the optical bandgap for Li-doped ZnO NSs samples, while a red shift is observed for Li-doped bulk ZnO samples. SEM images show flake-like nanostructures for Li-doped NSs and spherical shape particle-like structures for Li-doped bulk ZnO samples. The oxygen vacancies have been revealed by PL spectra, Zn K-edge XAFS, as well as XPS spectra. The band gap narrowing and widening were confirmed by the shift in valence band maxima for $\text{Zn}_{0.9}\text{Li}_{0.1}\text{O}$ bulk and $\text{Zn}_{0.92}\text{Li}_{0.1}\text{O}$ NSs. ZnO nanoflake structures have lots of fascinating exceptional properties such as large surface areas with porous structures. So, one can get improved performance and higher sensitivity in ZnO nanoflake structures-based sensors and solar cells for sensor devices where large surface areas are needed. On the other hand, the observed luminescence properties indicate possible application in the light emitting devices.

Acknowledgements MK is thankful to UGC DAE Consortium for Scientific Research, Indore for providing financial support as a research project (CSR-IC-ISUM-46/CRS-329/2020-21/787).

Declarations

Conflict of interest The authors declare no conflict of interest.

References

1. Yousefi R, Kamaluddin B (2009) *J Alloy Comp* 479:L11–L14
2. Feng Q, Liu J, Lu J, Mei Y, Song Z, Tao P, Pan D, Yang Y, Li M (2015) *Mater Sci Semicond Proc* 40:436
3. Liu CY, Xu HY, Sun Y, Ma JG, Liu YC (2014) *Opt Express* 22(14):16731
4. Giannouli M, Spiliopoulou F (2012) *Renew Energy* 41:115
5. Lany S, Osorio-Guillen J, Zunger A (2007) *Phys Rev B* 75:241203
6. Janotti A, Van de Walle CG (2007) *Phys Rev B* 76:165202
7. Shakti N, Devi C, Patra K, Gupta PS, Kumar S (2018) *AIP Adv* 8:015306
8. Saáedi A, Yousefi R, Jamali-Sheini F, Zak AK, Cheraghizade M, Mahmoudian MR, Baghchesara MA, Dezaki AS (2016) *Physica E* 79:113
9. Mahajan LM, Kasar CK, Patil DS (2019) *Mater Res Express* 6:045053
10. Saáedi A, Yousefi R, Jamali-Sheini F, Cheraghizade M, Zak AK, Huang NM (2013) *Superlattice Microstruct* 61:91

11. Zhang Z, Knutsen KE, Merz T, Kuznetsov AY, Svensson BG (2012) *Appl Phys Lett* 100:042107
12. Chawla S, Jayanthi K, Kotnala RK (2009) *Phys. Rev. B* 79:125204
13. Yavaş A, Güler S, Onak G, Erol M, Kayalar MT, Karaman O, Tunç ID, Oğuzlar S (2022) *J Alloy Compd* 891:162010
14. Alexandrov A, Zvaigzne M, Lypenko D, Nabiev I, Samokhvalov P (2020) *Sci Rep* 10:7496
15. Hou Q, Liu Y (2020) *Chem Phys* 531:110657
16. Yadav S, Jindal J, Mittal A, Sharma S, Kumari K, Kumar N (2021) *J Phys Chem Solids* 157:110217
17. Klingshirn C (2021) *Chem Phys Chem* 8:782
18. Lu JG, Zhang YZ, Ye ZZ, Zeng YJ, He HP, Zhu LP, Huang JY, Wang L, Yuan J, Zhao BH, Li XH (2006) *Appl Phys Lett* 89:112113
19. Chouhan L, Bouzerar G, Srivastava SK (2021) *J Mater Sci: Mater Electron* 32:6389
20. Chandekar KV, Shkir M, AlFaify S, Al-Shehri BM, Al-Namshah KS, Hamdy MS (2021) *J Mater Sci: Mater Electron* 32:3437
21. Chen X, Qingshuang X, Jitao Li (2020) *Ceram Int* 46:2309
22. Ariza R, Pavon F, Urbietta A, Fernandez P (2020) *J Phys Chem Solids* 139:109354
23. Meziane K, El Hichou A, El Hamidi A, Chhiba M, Bourial A, Almaggoussi A (2017) *Appl Phys A* 123:430
24. Lee W, Leem Jae-Young (2017) *J Nanosci Nanotechnol* 17:5697
25. Gurylev V, Perng TP (2021) *J Eur Ceram Soc* 41:4977
26. Punia K, Lal G, Dolia SN, Kumar S (2020) *Ceram Int* 46:12296
27. Quy CT, Thai NX, Hoa ND, Le DTT, Hung CM, Duy NV, Hieu NV (2018) *RSC Adv* 8:5629
28. He R, Tan B, Ton-Hhat C, Phillips M, Tsuzuki T (2013) *J Nanoparticle Res* 15:2030
29. Ortega PP, Silva CC, Ramirez MA, Biasotto G, Foschini CR, Simões AZ (2021) *Appl Surf Sci* 542:148723
30. Kumar P, Kumar A, Rizvi MA, Moosvi SK, Krishnan V, Duvenhage MM, Roos WD, Swart HC (2020) *Appl Surf Sci* 514:145930
31. Senol SD, Ozugurlu E, Arda L (2020) *J Alloy Compd* 822:153514
32. Kusiak-Nejman E, Wojnarowicz J, Morawski AW, Narkiewicz U, Sobczak K, Gierlotka S, Lojkowski W (2021) *Appl Surf Sci* 541:148416
33. Popa M, Pop LC, Schmerber G, Bouillet C, Ersen O (2021) *Appl Surf Sci* 562:150159
34. Dash D, Panda NR, Sahu D (2019) *Appl Surf Sci* 494:666
35. de Oliveira RC, Martins DE, Bernardi MIB, Mesquita A (2018) *Optical Materials* 86:71
36. Rana AK, Kumar Y, Rajput P, Jha SN, Bhattacharyya D, Shirage PM, *Appl ACS* (2017) *Mater Interfaces* 9:7691
37. Kumar S, Basu S, Rana B, Barman A, Chatterjee S, Jha SN, Bhattacharyya D, Sahoo NK, Ghosh AK (2014) *J Mater Chem C* 2:481
38. Kumar S, Tiwari N, Jha SN, Chatterjee S, Bhattacharyya D, Sahoo NK, Ghosh AK (2015) *RSC Advances* 5:94658
39. Rehr JJ, Mustre de Leon J, Zabinsky SI, Albers RC (1991) *J Am Chem Soc* 113:5135
40. Ravel B, Newville M (2005) *J Synch Rad* 12:537
41. Zabinsky SI, Rehr JJ, Ankudinov A, Albers RC, Eller MJ (1995) *Phys Rev B* 52:2995
42. Newville M, Boyanov B, Sayers DE (1999) *J Synchrotron Radiat* 6:264
43. Bilgin V (2009) *J Electron Mater* 38:1969
44. Fujihara S, Sasaki C, Kimura T (2001) *J Eur Ceram Soc* 21:2109
45. Kortüm G, Braun W, Herzog G (1963) *Angew Chemie Int Ed English* 2:333
46. Ivill M, Pearton SJ, Rawal S, Leu L, Sadik P, Das R, Hebard AF, Chisholm M, Budai JD, Norton DP (2008) *New J Phys* 10:065002
47. Schmid PE (1981) *Phys Rev B* 23:5531
48. Alaria J, Bieber H, Colis S, Schmerber G, Dinia A (2006) *Appl Phys Lett* 88:112503
49. Kamarulzaman N, Kasim MF, Rusdi R (2015) *Nanoscale Res Lett* 10:346
50. Dong CL, Persson C, Vayssieres L, Augustsson A, Schmitt T, Mattesini M, Ahuja R, Chang CL, Guo JH (2004) *Phys Rev B* 70:195325
51. Jullien M, Horwat D, Manzeh F, Galindo RE, Bauer P, Pierson JF, Endrino JL (2011) *Sol Energy Mater Sol Cells* 95:2341
52. Jeong E-S, Yu H-J, Kim Y-J, Yi G-C, Choi Y-D, Han S-W (2010) *J Nanosc And Nanotech* 10:3562
53. Teke A, Ozgur U, Dogan S, Gu X, Morkoc H, Nemeth B, Nause J, Everitt HO (2004) *Phy Rev B* 70:195207
54. Ozgur U, Alivov YI, Liu C, Teke A, Reshchikov MA, Dogan S, Avrutin V, Cho SJ, Morkoc H (2005) *J Appl Phys* 98:041301
55. Kumar PMR, Kartha CS, Vijayakumar KP, Singh F, Avasthi DK, Abe T, Kashiwaba Y, Okram GS, Kumar M, Kumar S (2005) *J Appl Phys* 97:013509
56. Agarwal DC, Chauhan R, Kumar A, Kabiraj D, Singh F, Khan S, Avasthi DK, Pivin J, Kumar M, Satyam P (2006) *J Appl Phys* 99:123105
57. Raji R, Gopchandran KG (2017) *J Sci Adv Mater Devices* 2:51
58. Chen M, Wang X, Yu YH, Pei ZL, Bai XD, Sun C, Huang RF, Wen LS (2000) *Appl Surf Sci* 158:134
59. Cong GW, Peng WQ, Wei HY, Han XX, Wu JJ, Liu XL, Zhu QS, Wang ZG (2006) *Appl Phys Lett* 88:062110
60. Kamarulzaman N, Kasim MF, Chayed NF (2016) *Results in Physics* 6:217

Publisher's note Springer Nature remains neutral with regard to jurisdictional claims in published maps and institutional affiliations.

Springer Nature or its licensor holds exclusive rights to this article under a publishing agreement with the author(s) or other rightsholder(s); author self-archiving of the accepted manuscript version of this article is solely governed by the terms of such publishing agreement and applicable law.